On the transition from Slow to Fast Wind as Observed in Composition Observations

B. L. Alterman¹, Y. J. Rivera², S. T. Lepri³, and J. M. Raines³

Space Science and Engineering
 Southwest Research Institute
 6220 Culebra Road
 San Antonio, TX 78238, USA
 e-mail: blalterman@swri.org
 Center for Astrophysics | Harvard & Smithsonian,
 60 Garden Street, Cambridge, MA 02138, USA
 University of Michigan
 Department of Climate and Space Sciences & Engineering Climate and Space Research Building

Received September 15, 1996; accepted March 16, 1997

2455 Hayward St.

Ann Arbor, MI, 48109, USA

ABSTRACT

Context. The solar wind is typically categorized as fast and slow based on the measured speed (v_{sw}). The separation between these two regimes is often set between 400 and 600 km s⁻¹ without a rigorous definition. Observations with v_{sw} above this threshold are considered "fast" and are typically considered to come from polar regions, i.e. coronal holes. Observations with v_{sw} below this threshold speed are considered "slow" wind and typically considered to originate outside of solar coronal holes. Observations of the solar wind's kinetic signatures, chemical makeup, charge state properties, and Alfvénicity suggest that such a two-state model may be insufficiently nuanced to capture the relationship between the solar wind and its solar sources. As heavy ion composition ratios are unchanged once the solar wind leaves the Sun, they serve as a key tool for connecting *in situ* observations to their solar sources. Helium (He) is the most abundance solar wind ion heavier than hydrogen (H). Long duration observations from the Wind Solar Wind Experiment (SWE) Faraday cups show that the solar wind helium abundance has two distinct gradients at speeds above and below $\sim 400 \text{ km s}^{-1}$. This is a key motivator for identifying the separation between fast and slow wind at such a speed.

Aims. We test this two-state fast/slow solar wind paradigm with heavy ion abundances (X/H) and characterize how the transition between fast and slow wind states impacts heavy ion in the solar wind.

Methods. We study the variation of the gradients of the helium and heavy ion abundances as a function of solar wind speed and characterize how the gradient of each abundance changes in fast and slow wind. We calculate v_{sw} as the proton or hydrogen bulk speed. The work uses *Advanced Composition Explorer* (ACE) heavy ion observations collected by the *Solar Wind Ion Composition Spectrometer* (SWICS) from 1998 to 2011. We compare the helium abundance observed by ACE/SWICS to the helium abundance observed by Wind/SWE to show the results are consistent with prior work.

Results. We show that (1) the speed at which heavy ion abundances indicate a change between fast and slow solar wind as a function of speed is slower than the speed indicated by the helium abundance; (2) this speed is independent of heavy ion mass and charge state; (3) the abundance at which heavy ions indicate the transition between fast and slow wind is consistent with prior observations of fast wind abundances; (4) and there may be a mass or charge-state dependent fractionation process present in fast wind heavy ion abundances.

Conclusions. We infer that (1) identifying slow solar wind as having a speed $v_{sw} \leq 400 \text{ km s}^{-1}$ may mix solar wind from polar and equatorial sources; (2) He may be impacted by the acceleration necessary for the solar wind to reach the asymptotic fast, non-transient values observed at 1 AU; and (3) heavy ions are fractionated in the fast wind by a yet-to-be-determined mechanism.

Key words. Solar wind (1534), Slow solar wind (1873), Fast solar wind (1872), Abundance ratios (11), Solar abundances (1474)

1. Introduction

The solar wind is a magnetized plasma originating in the solar atmosphere, where it is both energized and accelerated by the Sun before continuously flowing into and permeating interplanetary space. The class of surface feature from which a given solar wind stream emerges determines the acceleration and energization mechanisms and therefore profiles (Viall & Borovsky 2020). The variation in solar wind "types" or classes was first established from its bi-modal speed profile, observed

during solar minima from spacecraft with orbits in the ecliptic plane. However, Ulysses firmly established the difference between "fast" and "slow" wind when the spacecraft's passages over the Sun's polar regions revealed a markedly higher speed ($\nu_{\rm sw} > 400-500~{\rm km~s^{-1}}$ at latitude > 35°) compared to lower latitudes near the streamer belt (McComas et al. 2008; von Steiger et al. 2000). These results demonstrated that the higher speed wind observed—even in the ecliptic—originates from structures with continuously open magnetic field structures on the Sun (i.e. deep within coronal holes), while the slower speed wind

arose from closed field structures that are intermittently open to the heliosphere, such as active regions, helmet streamers, the Quiet Sun, and pseudostreamers (Fisk et al. 1999; Subramanian et al. 2010; Antiochos et al. 2011; Crooker et al. 2012; Abbo et al. 2016; Antonucci et al. 2005; Del Zanna 2019; Doschek & Warren 2019). The frequency at which various source regions occur and the regions on the Sun where they commonly occur varies with solar activity (McIntosh et al. 2015; Hewins et al. 2020; Wang & Sheeley 2002; Tlatov et al. 2014; Hathaway 2015). These variations with solar activity impact in situ observations at 1 AU, especially in regards to the occurrence rate of slow and fast wind along with the other features typically associated with them (Hirshberg 1973; Alterman & Kasper 2019; Alterman et al. 2021; Yogesh et al. 2023; McComas et al. 2008; Marsch 2006; D'Amicis & Bruno 2015; Zerbo & Richardson 2015; Schwenn 2006; Nicolaou et al. 2014; Du 2012; Lepri et al. 2013). However, the contribution of individual source regions to the slow solar wind and how these contributions change with solar cycle is still a major open question in heliophysics.

The solar wind becomes supersonic near the Sun where thermal energy is converted to kinetic energy (Parker 1958; Meyer-Vernet 2007). Above this height, it is further accelerated to an asymptotically faster speed during propagation through interplanetary space (Leer & Holzer 1980; Hansteen & Velli 2012; Holzer & Leer 1981, 1980; Johnstone et al. 2015). Broadly, the solar wind's asymptotic speed is a distinguishing characteristic of the variation of solar source regions. However within a small speed range, the solar wind can vary in density, temperature, Alfvénicity, chemical makeup, charge state population, and kinetic signatures, providing additional insight to its coronal origin and early development (von Steiger et al. 2000; Geiss et al. 1995b,a; Zhao et al. 2022; Xu & Borovsky 2015; Fu et al. 2017, 2015). The charge state and elemental composition of the solar wind are directly related to the temperature and density profiles of the solar source regions. Above a few solar radii, the charge state and elemental abundances remain fixed. As such, these two properties are distinguishing tracers of its solar origin (Xu & Borovsky 2015; Zhao et al. 2017a,b), which includes identifying the boundaries between solar wind streams of different origins as well as a means of identifying boundaries of transients (Zurbuchen & Richardson 2006; Richardson & Cane 2010). In other words, heavy ion observations provide a direct connection between in situ observations and the solar wind's properties at its solar origin. Rivera et al. (2022a) summarize the details of heavy ion properties at the Sun and in the solar wind.

Properties of elemental composition in the corona are observed to vary among neighboring coronal structures and often differ from the composition of the Sun's photosphere (Pottasch 1963; Feldman & Laming 2000; Widing & Feldman 2001; Brooks et al. 2015). A main elemental fractionation process is thought to be driven by the reflection and refraction of Alfvén waves at the chromosphere-corona boundary (Laming 2015). The resulting outward directed pondermotive force preferentially transport charged particles from the chromosphere to the corona while neutrals that are not yet ionized unaffected. Within the associated fractionation timescale, elements with a low first ionization potential (FIP < 11eV) are appreciably enhanced in the corona while those with high FIP (> 11eV) remain at photospheric levels. This is referred to as the "FIP effect". Because the behavior of this pondermotive force and the magnitude of its impact on elemental composition varies with magnetic topology at the Sun, elemental abundances measured at the Sun and heliosphere are directly linked to the fractionation phenomena across different source regions. In other words, elemental composition can indicate magnetic topology and field strength, thermal structure, and loop confinement duration, the latter of which is related to gravitational stratification (Raymond et al. 1997; Feldman & Laming 2000; Widing & Feldman 2001; Laming 2004, 2012; Weberg 2015; Rivera et al. 2022b; Baker et al. 2023; Mihailescu et al. 2023).

Ions heavier than He measured in the heliosphere exhibit strong FIP effect fractionation with slower speed wind being composed of a range of low-FIP enhanced plasma (by factors of greater than 3) while fast speed wind converges to abundances more similar to the Sun's photospheric composition (von Steiger et al. 2000). The "FIP bias" is the ratio of high FIP abundances to low FIP abundances. Polar passes of Ulysses observations find that the fast solar wind has a steady ion and elemental composition while the slow solar wind can reflect fast wind characteristics as well (Stakhiv et al. 2015). The slow wind was subcharacterized as typical slow wind and boundary wind where the boundary wind contained ionic composition similar to slow wind but elemental composition resembling fast wind. The heavy ion variability of the slow wind is also observed on the ecliptic plane with ACE/SWICS observations (Livi et al. 2003). Similarly, the ion composition $(O^{7+}/O^{6+}, C^{6+}/C^{5+}, C^{6+}/C^{5+})$ have been used as tracers of solar wind origin back the Sun (Zhao et al. 2017b). When organized by bulk speed, the O^{7+}/O^{6+} ratio has a large overlap between traditionally fast (coronal hole) and slow wind (active region, Quiet Sun, helmet streamers) sources suggesting the slow wind, as defined by ion ratios, is formed across various sources. The variability in the compositional makeup of the slower speed wind suggests many distinct solar sources.

The helium abundance ($A_{\rm He}$) is the hydrogen-to-helium number density ratio. Often, it is expressed in units of percent (Aellig et al. 2001; Kasper et al. 2007, 2012; Alterman & Kasper 2019; Alterman et al. 2021; McIntosh et al. 2011) $A_{\rm He}$ exhibits the most extreme values in coronal mass ejections, sometimes reaching over 20% (Song et al. 2020; Johnson et al. 2024). Helium is generally in the form of He²⁺ after leaving the corona, however occasionally measurements in the solar wind measure significant amount of He⁺ that is believed to have originated at the Sun (Rivera et al. 2020). Categorizing $A_{\rm He}$ by $v_{\rm sw}$ provides more nuanced insight.

Broadly, solar wind helium observations from the Wind spacecraft aggregated across several solar cycles show helium abundances gradually increase with increasing solar wind speed up to $\sim 400 \text{ km s}^{-1}$ and then saturates to $\sim 4\%$ (Aellig et al. 2001; Kasper et al. 2006; Alterman & Kasper 2019; Yogesh et al. 2021). We define the solar wind speed as the hydrogen bulk speed. This dependence of A_{He} on v_{sw} is stronger in slower solar wind and during solar activity minima (Aellig et al. 2001). It also varies with heliographic latitude and, accounting for this heliographic variability, the gradient of $A_{\rm He}$ as a function of $\nu_{\rm sw}$ in slow wind is linear (Kasper et al. 2007). Both the heliographic and v_{sw} dependencies are absent during solar maxima, suggesting that slow solar wind helium has two distinct sources: the streamer belt and active regions (ARs) (Kasper et al. 2007). Furthermore, the speed at which helium vanishes from the solar wind is $v_v = 259 \pm 12 \text{ km s}^{-1}$, which is within 1σ of the minimum observed solar wind speed, and may be related to how helium interacts with solar wind acceleration (Kasper et al. 2007) and is robust to analysis across multiple solar activity cycles (Alterman & Kasper 2019). Extending the analysis of A_{He} to multiple solar cycles shows that $A_{\rm He}$'s variability with solar activity carries a v_{sw}-dependent phase lag (Feldman et al. 1978; Alterman & Kasper 2019), which is likely driven by changes in distinct slow solar wind source regions, i.e. helmet streamers and ARs. A_{He} 's

 $v_{\rm sw}$ -dependence also shows a rapid depletion or "shutoff" approximately 250 days prior to solar minima across multiple solar activity cycles, which may be related to changes in the magnetic topology of solar wind source regions (Alterman et al. 2021).

Heavier elements (Z > 2) observed in the ecliptic at 1 AU also express speed and solar cycle dependence which can provide additional insight to the transitional boundaries observed with He (Lepri et al. 2013). Combining A_{He} with C^{6+}/C^{5+} and O⁷⁺/O⁶⁺ ratios shows that the temperature of slow wind solar wind source regions also varies with solar activity, decreasing with decreasing sunspot number (SSN) (Kasper et al. 2012). Extending the analysis to Fe/O, McIntosh et al. (2011) infer that a decrease in plasma heating deep in the solar atmosphere during solar minima drives the decrease in $A_{\rm He}$ with decreasing solar activity. Extending this abundance analysis to additional element ratios and using H-normalized abundances (X/H), Lepri et al. (2013) show X/H vary with solar activity in the same manner as heavy ion charge state ratios for both fast and slow solar wind, which further ties the variability of solar wind observations at 1 AU to changes in solar wind source region properties. Clearly, examining a range of elements of a large range of chemical properties (e.g. mass and FIP) will enable a more rigorous characterization of source region and solar wind release because those properties impact a given element's interaction with source region and solar wind release processes.

In this work, we extend the analysis of Aellig et al. (2001); Kasper et al. (2007, 2012); Pilleri et al. (2015); Alterman & Kasper (2019); Alterman et al. (2021) to examine the dependence of heavy ion composition on solar wind speed using Advanced Composition Explorer's (ACE; Stone et al. 1998) Solar Wind Ion Composition Spectrometer (SWICS; Gloeckler et al. 1998) over the years 1998 to 2011. To enhance our confidence in these results, we compare our observations of the helium abundance observed by ACE/SWICS to the same abundance observed by the Faraday cups that are part of the Wind spacecraft's Solar Wind Experiment (SWE; Ogilvie et al. 1995). This paper proceeds as follows. Section 2 briefly summarizes our observations. Section 3 presents our analysis. In Section 4, we discuss the results. Section 5 then concludes.

2. Observations

We use data from both a Faraday cup (FC) and a mass spectrometer. They are on distinct instruments, both at the 1st Earth-Sun Lagrange point (L1), but onboard different spacecraft. Section 2.1 of Verscharen et al. (2019) summarizes the classes of instruments in detail. Here, we identify the specific instruments, datasets, and data selection used.

2.1. Wind/SWE Faraday Cup Observations

We use observations of the solar wind speed (v_{sw}), hydrogen density, and helium density provided by the Wind (Acuña et al. 1995) Solar Wind Experiment (SWE, Ogilvie et al. 1995) Faraday cups (FCs). These observations are provided by CDAWeb at the native \sim 92s cadence. There are multiple SWE data sets, each each utilizing non-linear fitting to extract physical parameters, and optimized for different objectives (Kasper et al. 2006; Maruca & Kasper 2013; Alterman et al. 2018) We use the data optimized for deriving the helium abundance, which is described by Kasper et al. (2006); Kasper (2002). This dataset only considers one proton population, which is nominally the proton core (Alterman et al. 2018). Our data selection follows Alterman & Kasper (2019); Alterman et al. (2021).

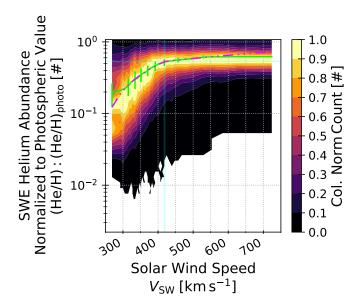


Fig. 1. A contour plot corresponding to a column-normalized 2D histogram of the SWE helium abundance as a function of the proton speed observed at *Wind*. The solid green line and error bars are the mean and standard deviation in each column. The pink dash-dotted line show the result of bi-linear fit to the green line, where each line is selected as the minimum of both lines in the bi-linear function over the full domain. Only speed $v_{\rm sw} > 300~{\rm km~s^{-1}}$ are included in the fit. Semi-transparent blue lines indicate the saturation speed (v_s) and saturation abundance (A_s) along with their uncertainties, where the bi-linear function changes slope.

2.2. ACE/SWICS Observations

The Advanced Composition Explore (ACE, Stone et al. 1998) Solar Wind Ion Composition Spectrometer (SWICS, Gloeckler et al. 1998) is an energy - time-of-flight mass spectrometer that provides heavy ion composition observations of H, He, C, N, O, Ne, Mg, Si, S, Fe at 2hr cadence (Shearer et al. 2014). For ACE observations of H and He, we utilize data from the auxiliary channel of ACE/SWICS (Lepri et al. 2013). For ACE observations of H, we utilize data from the auxiliary channel of ACE/SWICS, a separate ESA channel of the instrument that is optimized for H observations (Lepri et al. 2013). Density and velocity are calculated from the first and second moments and then quality filtered, effectively eliminating contamination from the small amount of He present. We limit our study to the years 1998 to 2011, i.e. data from before SWICS' detector anomaly (Zurbuchen et al. 2016). To isolate ambient and non-transient solar wind, we remove interplanetary coronal mass ejections (ICMEs; Richardson & Cane 2010) and corotating interaction regions (CIRs; Mason et al. 2012).

3. Analysis

3.1. The Fast/Slow Transition

The categorization of solar wind by speed into "fast" and "slow" can be considered overly broad and requires both reconsideration and additional detail. In this section, we utilize observations over the full range of ν_{sw} observed by Wind/SWE to characterize the speed at which the helium abundances changes from characteristically "slow" to characteristically "fast".

Figure 1 the SWE helium abundance as a function of the proton speed observed at *Wind*. The abundance is normalized to its

photospheric value (Asplund et al. 2021). The proton speed is binned in 45 quantiles over the range 250 to 800 km s⁻¹. Visual inspection shows that there is a point around ~ 400 km s⁻¹ where the slope of He/H as a function of $v_{\rm sw}$ decreases. Because quantiles divide the data into intervals with an equal number of observations and slower speeds are observed more frequently than faster speeds, quantiles provide greater resolution around the saturation speed v_s than fixed width intervals would. We have normalized the observations in each column to the column's maximum value so that the overall trend of He/H with $v_{\rm sw}$ is not obscured by the $v_{\rm sw}$ sample frequency and this point is easily seen on inspection.

To quantify this transition, we have fit the trend of these distributions with the bi-linear function

$$A(v) = \min \left[A_1(v), A_2(v) \right] = \min \left[m_1(v - v_1), m_2(v - v_2) \right]. \tag{1}$$

A(v) is the abundance normalized to its photospheric value

$$A = (X/H): (X/H)_{\text{photo}}, \qquad (2)$$

where $X/H = n_X/n_H$ is the number density of species X normalized to the H number density. For the two lines indicated by subscript 1 or 2, A_i are the two different lines; m_i are the slopes of the lines, and v_i are the x-intercepts of the lines. Kasper et al. (2007) calls v_i for the line in Equation (1) with the steeper slope (nominally the slow wind) the vanishing speed, i.e. the speed at which A_{He} vanishes from the solar wind. The two lines intersect at the saturation speed (v_s) where the abundances of both lines are equal $A_1 = A_2 = A_s$. The speed at the intersection between the two lines in Equation (1) is given by

$$v_{\rm s} = \frac{m_2 v_2 - m_1 v_1}{m_2 - m_1}. (3)$$

As the intersection of two lines reduces the number of free parameters in the two equations to four, we choose to parameterize the fit function so that the free parameters are v_s , A_s , v_1 (the x-intercept of the $v < v_s$ line), and m_2 (the slope of the $v > v_s$ line). This parameterization directly quantifies the point at which He/H transitions from its slow to fast wind values (v_s , A_s) and provides uncertainties for it. To account for the variable frequency with which Wind samples different solar speeds and reduce the impact of extreme values of He/H, we select data in bins within 80% of the column maximum and then calculate the mean and standard deviation in log-space. We then fit these mean values with the minimum of two lines Equation (1). Each column's standard deviation is used as the weight. The green line and error bars in Figure 1 show the mean and standard deviation in each column. The pink dash-dotted line shows the trend. As He/H saturates to its fast wind value $A_s = 0.520 \pm 0.004$ at speeds $v > v_s = 399 \pm 2 \text{ km s}^{-1}$, we refer to this as the saturation speed v_s and the corresponding abundance A_s as the saturation abundance. We refer to this coordinate (v_s, A_s) as the "saturation point". Although it has been suggested to refer to this point as a transition, that would imply the symbol v_t , which could easily be confused with the thermal speed.

Solar wind acceleration and heating leave signatures in the trends of heavy ions observed at 1 AU. To characterize the impact of these signatures on the transition between "slow" and "fast" wind, we have examined the SWICS abundances of He, C, N, O, Ne, N, Mg, Si, S, and Fe all normalized to hydrogen (X/H) in the same manner as He/H observed by SWE in Figure 1. Figure 2 plots these SWICS and SWE abundances as a function of v_{sw} observed at their respective spacecraft. We limit

the observations plotted to those below 600 km s^{-1} because Figure 1 shows the transition is at speeds more than 100 km s^{-1} slower and due to large scatter at higher speeds. Every second data point is marked. Labels on the right side of the plot indicate the species, with *SWE* indicating He/H observed by Wind/SWE.

We have fit the plotted observations with the bi-linear function in Equation (1). Vertical, semi-transparent lines in Figure 2 indicate the speeds at which the slope of the bi-linear fit changes, i.e. each species' saturation speed. Table 1 gives saturation speeds (v_s) and abundances (A_s) along with the other parameters for the fits and the percentage of the observations in the $v < v_s$ regime. This latter quantity shows that the slow wind portion of each species contains a non-trivial fraction of that species' observations. Although there is more scatter in the plots due to SWICS' lower time resolution and the time period over which observations are available is smaller, they all show a fast-to-slow transition. Excluding He, the average heavy ion saturation speed is $v_s = 327 \pm 2 \text{ km s}^{-1}$. We have performed a similar average for the low and high FIP elements and those v_s are the same to with in the propagated uncertainties. Broadly, all species show similar qualitative behavior in that all X/H monotonically increase with increasing v_{sw} and have a different gradients at speeds above and below their respective v_s .

To better characterize these gradients, Figure 3 re-plots the data in Figure 2 and scales the observations to the saturation point (v_s, A_s) , which is plotted at (1, 1). He for SWE and SWICS do not extend to as large of a value on the x-axis as other species because $v_{s,\text{He}}$ is larger than $v_{s,\text{Heavy}}$. This figure shows that below the saturation speed $(v < v_s)$, the gradient of scaled abundances as a function of v_{sw} is indistinguishable across the different species. For speeds $v > v_s$, each species' gradient is shallower than its $v < v_s$ gradient and these gradients are different for the different species. C, N, and O have the steepest gradients that are most similar to their $v < v_s$ gradient. Fe and He have the shallowest gradients that are most distinct from their $v < v_s$ gradient. Ne, Mg, Si, and S are the intermediate case.

3.2. Saturation Properties

In this section, we characterize the saturation of each species at its (v_s, A_s) point. The figures Figures 4 to 6 use a consistent style in which each species' color and marker match its style in Figures 2 and 3. Data points are connected with a black dotted line to aid the eye. The top axis indicates the species. In the case of He/H from SWE, the marker is explicitly labeled to differentiate it from SWICS' He/H.

Figure 4 plots v_s as a function of FIP. The vertical dashed line is 11 eV, the nominal change between high and low FIP (Alterman et al. 2023). It shows that v_s for all heavy ions are within the 1σ fit uncertainty of each other. Ne is the exception in that the upper range of $v_{s,\rm Ne}$ is slower than the lower range of $v_{s,\rm Si}$. Excluding He, the average saturation speed for heavier elements is $v_s = 327 \pm 2 \, \mathrm{km \, s^{-1}}$. The He/H saturation speed observed by SWICS is $v_s = 390 \pm 4 \, \mathrm{km \, s^{-1}}$. For comparison, v_s for He/H observed by SWE is $v_s = 399 \pm 2 \, \mathrm{km \, s^{-1}}$, a 3 to 15 km s⁻¹ difference, which we consider small in comparison to the $63 \pm 4.5 \, \mathrm{km \, s^{-1}}$ difference between v_s for SWICS' He/H and heavier elements.

Figure 5 plots the saturation abundance A_s as a function of FIP. Again, the vertical dashed line indicates 11 eV, the nominal transition between low and high FIP. This figure shows the expected rend that low FIP elements (FIP < 11 eV) are enhanced more than high FIP elements by a factor of approximately 2. This trend is expected from Zurbuchen et al. (2016), who compared

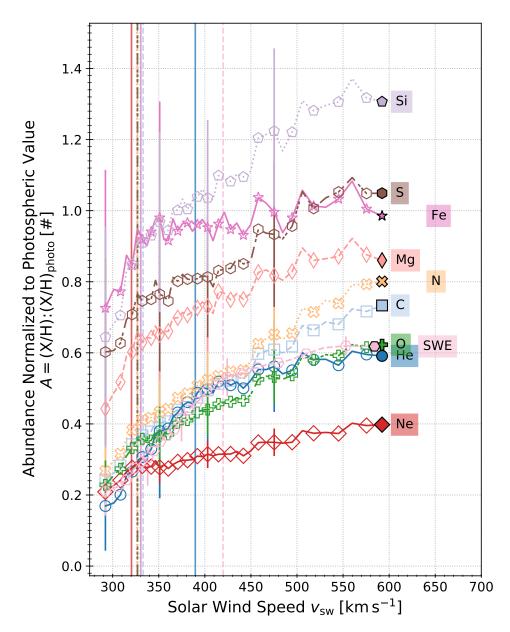


Fig. 2. Abundances averaged in solar wind speed bins. Saturation speeds (v_s) are indicated by vertical lines of the corresponding color. The species are indicated on the right hand side of the plot. The SWE observations of A_{He} from Figure 1 are shown for reference in pink hexagons and labeled *SWE*. Only every second bin is marked for visual clarity.

X/O in interplanetary coronal mass ejections (ICMEs), fast solar wind, and slow solar wind. That S behaves like a low FIP element is also consistent with observations of suprathermal ions during quiet times (Alterman et al. 2023).

To characterize the change in gradients for speeds $v > v_s$, we have normalized the abundance at 592 km s⁻¹, which is the fastest considered in this analysis and are filled markers in Figures 2 and 3, to A_s and plotted it as a function of element mass (M) in Figure 6. Normalizing to A_s removes the photospheric normalization. We choose M because these quantities are not organized by FIP and several M-dependent fractionation processes have been observed (Rivera et al. 2021; Lepri & Rivera 2021; Pilleri et al. 2015; Weberg et al. 2012; Wurz et al. 2000). Table 1 includes the abundances at 592 km s⁻¹ under A (592 km s⁻¹). Normalizing this fastest abundance to A_s allows us to qualitatively characterize the gradient in a manner that accounts for the known differences in heavy ion abundances due to frac-

tionation processes in the chromosphere and transition region (Laming 2004, 2009, 2015; Schwadron et al. 1999; Geiss 1982; Geiss et al. 1995a). Error bars are the propagated errors including the fit uncertainty in A_s and the statistical uncertainty in the 592 km s⁻¹ data point. Excluding He, which is a known outlier in comparison to heavier elements, we observe a roughly monotonic decreases in $A(592 \text{ km s}^{-1})/A_s$ with three clusters. C, N, and O are clustered in the range ~ 1.8 to 2. Mg, Ne, Si, and S are clustered at ~ 1.5 . Fe's $A(592 \text{ km s}^{-1})/A_s$ is approximately 1.2, which is comparable to He's.

4. Discussion

Broadly, the solar wind can be classified into two types based on its speed: fast and slow. The difference between fast and slow wind is often chosen *ad hoc* to be somewhere in the range of $400 \text{ to } 600 \text{ km s}^{-1}$. For example, an often cited justification for

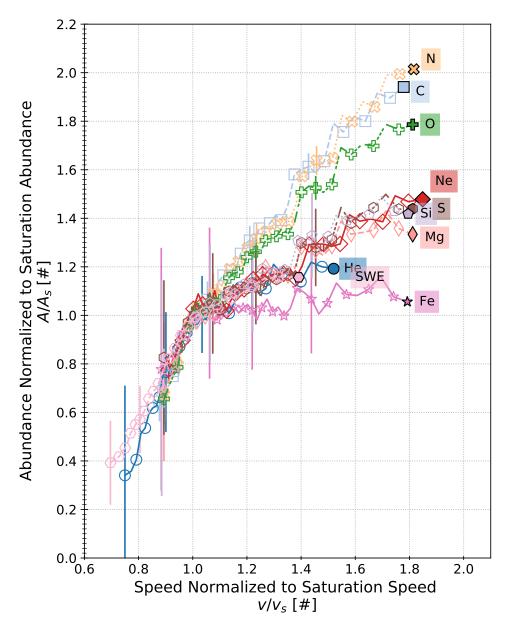


Fig. 3. Observations plotted in Figure 2, but scaled to their (v_s, A_s) values, which is plotted at (1, 1).

classifying the solar wind as fast or slow is that the helium abundance has a strong, positive gradient with solar wind speed in slow wind and saturates to a fixed value in fast wind. We identify the speed-abundance pair at which a given element transitions from slow wind-like to fast wind-like behavior as (v_s, A_s) by fitting Equation (1) to the trends of X/H as a function of v_{sw} . Using several solar cycles of observations from the Wind Faraday cups, Figure 1 shows that, statistically, He/H saturates to a photospheric-normalized abundance of $A_s = 0.520 \pm 0.004$ at $v_s = 399 \pm 2 \text{ km s}^{-1}$. However, in situ observations of kinetic properties (Kasper et al. 2008, 2017; Tracy et al. 2016; Alterman et al. 2018; Klein et al. 2018; Martinović et al. 2020, 2021), chemical makeup and charge state properties (von Steiger et al. 2000; Geiss et al. 1995b,a; Zhao et al. 2017a, 2022; Xu & Borovsky 2015; Fu et al. 2017, 2015), and cross helicities (Tu & Marsch 1995; Bruno & Carbone 2013; D'Amicis et al. 2021a) indicate that the helium abundance alone carries insufficient information to fully characterize the transition between fast and slow solar wind.

We repeat the analysis in Figure 1 for all heavy ion abundances X/H observed by ACE/SWICS, both He and heavier elements. Figure 2 plots the observations. Figure 4 summarizes the derived saturation speeds v_s as a function of FIP. In the case of SWICS' He/H, the abundance saturates to it's fast wind value at $v_s = 390 \pm 3 \text{ km s}^{-1}$, which is at most 14 km s⁻¹ slower than v_s observed by Wind/SWE. Figure 4 shows that, with the exception of Ne and Si, heavy element v_s are all within their mutual uncertainties. As such, we take their weighted mean $v_s = 327 \pm 2 \text{ km s}^{-1}$ as the typical heavy element saturation speed, which is indicated by a horizontal blue line in Figure 4. This heavy ion v_s is 63 ± 5 km s⁻¹ slower than v_s observed by SWICS, which is $7 \times$ larger than the difference between v_s observed by SWICS and SWE for He/H. Given that SWICS is a time-of-flight mass spectrometer, SWE consist of two Faraday cups, and these two instruments are mounted on different spacecraft, a difference of < 4% between v_s derived form SWICS and SWE measurements seems negligible in comparison to the difference between v_s for He and heavier elements observed by

	Vanishing	Saturation	Saturation	Fast Wind	Fastest	Slow Wind
	Speed	Speed	Abundance	Slope	Abundance	Observations
	v_{v}	v_s	A_s	m_i	$A(592 \mathrm{km}\mathrm{s}^{-1})$	$v < v_s$
	$[{\rm km}{\rm s}^{-1}]$	$[{\rm km}{\rm s}^{-1}]$	[#]	$[\% \text{km}^{-1} \text{s}]$	` [#]	[%]
SWE	237 ± 6	399 ± 2	0.520 ± 0.004	0.00045 ± 0.00003	0.60 ± 0.04	50
He	243 ± 3	390 ± 4	0.496 ± 0.009	0.00055 ± 0.00007	0.59 ± 0.09	44
C	220 ± 7	333 ± 7	0.378 ± 0.013	0.00152 ± 0.00005	0.73 ± 0.10	18
N	224 ± 6	326 ± 4	0.398 ± 0.008	0.00158 ± 0.00004	0.80 ± 0.13	17
O	228 ± 6	327 ± 4	0.349 ± 0.008	0.00115 ± 0.00004	0.62 ± 0.07	18
Ne	196 ± 17	320 ± 4	0.269 ± 0.004	0.00048 ± 0.00002	0.40 ± 0.03	18
Mg	221 ± 13	327 ± 5	0.645 ± 0.011	0.00108 ± 0.00007	0.86 ± 0.18	17
Si	214 ± 12	330 ± 4	0.921 ± 0.015	0.00178 ± 0.00008	1.31 ± 0.48	17
S	156 ± 45	327 ± 10	0.729 ± 0.018	0.00132 ± 0.00008	1.05 ± 0.30	14
Fe	168 ± 34	331 ± 6	0.933 ± 0.012	0.00034 ± 0.00009	0.99 ± 0.37	16
Avg	221 ± 3	327 ± 2	0.383 ± 0.003	0.00083 ± 0.00001	_	_
Low FIP	212 ± 8	329 ± 3	0.795 ± 0.007	0.00115 ± 0.00004	_	
High FIP	223 ± 4	326 ± 2	0.302 ± 0.003	0.00079 ± 0.00002	_	

Table 1. Saturation speeds and abundances along with the slow wind x-intercept (v_v , vanishing speed) and fast wind slope (m_i). These parameters characterize the fits to Equation (1). The abundance observed at 592 km s⁻¹ is given by A (592 km s⁻¹). All abundances are normalized to their photospheric value. SWE is He/H observed at *Wind*. The average value is calculated excluding SWE and SWICS He/H. High and Low FIP averages exclude He/H as well. Percentage of data in slow wind regions ($v < v_s$) shows that non-trivial portions of the observations occur at these speeds.

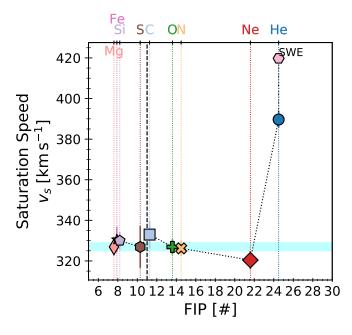


Fig. 4. The saturation speed (v_s) as a function of first ionization potential (FIP). The vertical dashed line is 11 eV, the nominal change between high and low FIP. The semi-transparent, horizontal blue bar indicates the weighted average of $v_s = 327 \pm 2$ km s⁻¹ for elements heavier than He. To within their mutual uncertainties, all but Ne and Si have the same v_s .

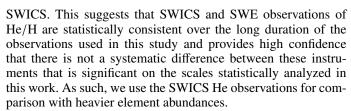


Figure 5 plots the saturation abundance A_s , the abundances at v_s , as a function of FIP and shows the expected dependence.

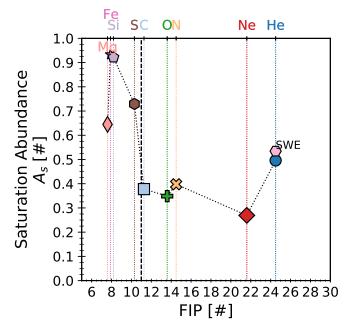


Fig. 5. Each element's saturation abundance (A_s) as a function of FIP. The vertical dashed line is 11 eV, the nominal change between high and low FIP. The $\sim 2 \times$ difference between low and high FIP abundances is expected.

In qualitative with Zurbuchen et al. (2016); Von Steiger & Zurbuchen (2016), low FIP elements are enhanced from their photospheric values by $\sim 2 \times$ more than high FIP elements. The agreement is qualitative because Zurbuchen et al. (2016); Von Steiger & Zurbuchen (2016) analyze X/O or normalize their X/H values to fast wind X/H, not photospheric values. The observed FIP-dependence suggests the unsurprising result that the abundances characteristic of the transition between slow and fast solar wind are driven in chromosphere, where solar wind abundances are fractionated by the pondermotive force (Laming 2004, 2009,

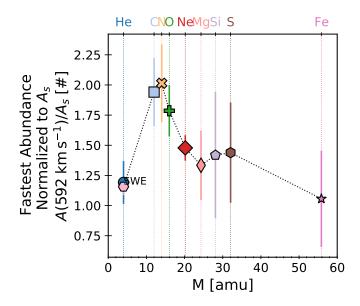


Fig. 6. The abundance at $v_{\rm sw} = 592 \ {\rm km \, s^{-1}}$ normalized to A_s as a function of element mass. Excluding He, the decreasing trend with increasing M indicates a heavy ion fractionation process in fast solar wind.

2015; Schwadron et al. 1999; Geiss 1982; Geiss et al. 1995a). For completeness, we have also examined these saturation abundances as a function of element mass (M) and typical solar wind charge state (Q) (von Steiger et al. 1997; Desai et al. 2006). Although beyond the scope of this paper and not shown for space, we note that A_s for high FIP elements shows a monotonic decrease with increasing M and Q.

To contextualize the gradients of X/H as a function of v_{sw} at speeds slower and faster than v_s , Figure 3 scales the observations plotted in Figure 2 to each species' transition point (v_s, A_s) . As abundance are set by FIP in the chromosphere and the solar wind's asymptotic speed is set above this height, such a normalization removes any (simple) offsets that are due to preferential element or ion coupling to these mechanisms and reveals any trends obscured by them. This shows that in solar wind with speeds $v < v_s$, the gradients of X/H as a function of v_{sw} are effectively indistinguishable. This is not the case for speeds $v > v_s$, for which there may be three distinct groups. For high FIP elements heavier than He (i.e. C, N, and O), the change in gradient at $v > v_s$ is least significant. Low FIP elements Mg, Si, and S have an intermediate change in gradient. Ne and Fe are the exceptions to this trend. Although Ne is high FIP, the change in its gradient is more similar to the low FIP elements than other high FIP elements. In the case of Fe, its gradient at $v > v_s$ is most similar to He, which is generally an exception to composition trends. Figure 6 plots the fastest reported abundance at 592 km s⁻¹, the fastest speed plotted in Figure 2 and indicated by filled markers, normalized to A_s as a function of mass and shows that, with the exception of He, these transition abundances A_s are well-ordered by mass, indicating a possible mass-dependent fractionation process in solar wind with $v > v_s$.

4.1. Implications for the Fast/Slow Solar Wind Transition and Solar Wind Sources

Coronal conditions are such that energy conversion at the sonic point is insufficient to yield the asymptotic fast wind speeds observed at 1 AU (Leer & Holzer 1980; Hansteen & Velli 2012). Rather, additional energy must be supplied to the solar wind to

achieve the asymptotically fastest observed non-transient solar wind. In contrast to a quantity that evolves with distance like speed, elemental abundances are conserved quantities. This is key to utilizing FIP fractionation as an *in situ* diagnostic of solar wind source regions at the Sun. The combined measurements of abundances and speed therefore probe a combination of solar wind source region and transport effects.

The overall trends of X/H with v_{sw} that show two distinct gradients at speeds $\langle v_s \text{ and } \rangle v_s$ in Figures 2 and 3 are consistent with the two-state solar wind paradigm under which fast wind is from coronal holes (CH) with magnetic fields that are continuously open to heliosphere and slow wind is from equatorial sources with more complex, likely intermittently open magnetic topologies. The difference between low and high FIP A_s in Figure 5 is consistent with Figure 5 in Zurbuchen et al. (2016) and a FIP-dependent process at the Sun fractionating elemental abundances in the chromosphere, which suggests that the fast/slow transition is independent of the FIP effect. Given that v_s is similar for all elements heavier than He and the solar wind speed is set above heights where FIP fractionation occurs, we make the unsurprising inference that the transition between fast and slow solar wind sources occurs at heights above where the pondermotive force or any similar process that induces fractionation impacts the solar plasma. The difference in He v_s and heavy element v_s along with the difference in gradients of X/Hat speeds below and above v_s require a more nuanced interpreta-

Two critical distances associated with solar wind acceleration are the sonic and Alfvén critical point, which we denote by r_c and r_A , respectively. The sonic point is the distance from the Sun's surface at which the solar wind's bulk speed exceeds the thermal speed. Under the Parker model (Parker 1958), this happens when the plasma's thermal energy is converted to kinetic energy and the solar wind becomes supersonic. The Alfvén point or surface is the distance at which the solar wind's speed exceeds the local Alfvén speed, i.e. the solar wind is traveling faster than information can propagate along magnetic field lines attached to the Sun's surface. Kasper et al. (2021) observed the Alfvén surface to be just below 20 R_S . Alfvén waves are a possible source of the energy above either r_c and/or r_A necessary for the solar wind to achieve its asymptotic fast wind values.

Our analysis assumes that there exists a characteristic point (v_s, A_s) for each species' abundance as a function of v_{sw} and this point statistically indicates a transition between measurements of plasma from CH and equatorial sources that each have characteristic speeds, abundances, and abundance gradients as a function of v_{sw} . By normalizing the observed trends in Figure 2 to this point (v_s, A_s) , Figure 3 accounts for any offsets present in these trends that, by assumption, are unrelated to the process(es) that lead to the two different gradients above and below v_s . Because the gradients for $v < v_s$ are consistent across species, we infer that there is no process that preferentially couples to and drives changes in any one species abundances or as a function of a element properties like M, Q, M/Q, or FIP. In other words, there is no fractionation process in the slow wind beyond that which is introduced by the FIP effect in the chromosphere, as observed by the vertical scaling in Figure 2.

To contextualize the difference in v_s for He and heavier elements, Figure 7 plots these speeds with the probability density of $v_{\rm sw}$ observations from SWICS. Vertical green lines indicate v_s for He observed by SWICS and the weighted average of v_s for heavier elements; line widths are the range of values covered by the uncertainties. The vertical dotted line is the peak of the $v_{\rm sw}$ distribution. This visualization clearly shows that $v_{s, {\rm He}} > v_{s, {\rm Heavy}}$

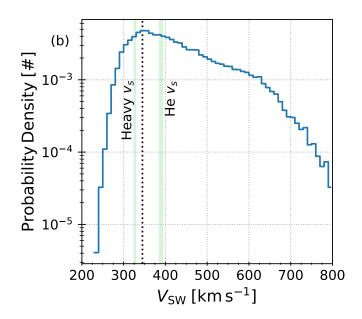


Fig. 7. Probability density of $v_{\rm sw}$ observed by SWICS and SWE. The vertical green lines are saturation speeds v_s including uncertainty. The vertical black dotted line is the peek solar wind speed bin, $v_{\rm sw}=345~{\rm km~s^{-1}}$.

and these two characteristic speeds are separated by the solar wind distribution's peak. Using SWE observations of v_{sw} and He/H does not change this interpretation. That v_s for elements heavier than He are mutually consistent further suggests that there is no process that preferentially accelerates heavier elements at distances from the Sun $> r_c$ or $> r_A$, where processes that occur during transport continue to accelerate the fast solar wind to its asymptotic values. However, this does not rule out such an *in situ* acceleration process impacting He for $v > v_s$. For example, He's large density with respect to heavier elements makes it more likely to be impacted by beam instabilities, interparticle Coulomb collisions, and Alfvén wave transport. If the difference between $v_{s,He}$ and $v_{s,Heavy}$ is due to in situ an acceleration process at distances from the Sun above the sonic point r_c preferentially coupling to He in comparison to heavier elements, the difference between $v_{s,He}$ and $v_{s,Heavy}$ has profound implications for the definitions of fast and slow solar wind.

The helium abundance is a key motivator for associating fast and slow solar wind to with distinct solar sources. The scaled observations in Figure 3 show that $X/H(v < v_s)$ have indistinguishable gradients. Figures 2 and 5 show the expected FIP fractionation. From this, we infer that observations from $v < v_s$ are equatorial in origin and observations from $v > v_s$ are CH in origin. A consequence of this that differentiating between fast and slow solar wind with a threshold in the range of 400 to 600 km s⁻¹ would yield "slow wind" abundances with chemical compositions reflecting a mixture of source regions continuously magnetically open to the heliosphere (e.g. CHs) and those that are only intermittently open (i.e. equatorial sources). Such a mixing would obscure our ability to properly map slow solar wind back to its solar origin.

4.2. Implications for Fast Wind Fractionation and Solar Wind Acceleration

Pilleri et al. (2015) study heavy ion abundances normalized to Mg during solar minimum 23 and maximum 24 using

ACE/SWICS data to contextualize Genesis observations (Burnett et al. 2003). They divide their observations into those from CHs, equatorial sources, and CMEs; calculate their abundances with respect to magnesium; and include an analysis of X/Mg's dependence on v_{sw} . They divide their solar wind observations into CH and equatorial in origin based on a change in solar wind speed. They report mass-dependent fractionation trends comparable to ours where by O/Mg, C/Mg, and He/Mg show two distinct gradients above and below $\sim 400 \text{ km s}^{-1}$, which roughly divides equatorial and CH wind. That their threshold speed is faster than v_s we report for heavy ions is unsurprising because they separate CH and equatorial solar wind by following Reisenfeld et al. (2013) and setting a threshold on solar wind speed at stream interfaces that is 425 km s⁻¹ for rarefaction regions and 525 km s⁻¹ compression regions. These authors also attribute their fractionation to a secondary dependence of the pondermotive force predicted by Laming (2004). However, Laming (2004, 2009, 2015) emphasize that the pondermotive force is effectively mass-independent. As such, another explanation may be necessary.

One possibility is that the solar wind speed varies between the center and boundary of CHs (Zhao et al. 2017a). Performing a superposed epoch analysis of 66 Carrington rotation long intervals of CH solar wind, Borovsky (2016) shows a gradient of speed in time over the range of 400 to 600 km s⁻¹, which is the range over which we observe an enhancement in $A \left(592 \text{ km s}^{-1}\right)/A_s$. However, Borovsky (2016) also shows that Fe/O does not vary over these intervals. As the abundance normalized to A_s of Fe/H has the shallowest gradient for speeds $v > v_s$ and that of O/H has one of the strongest gradients, this suggests that our observed mass fractionation is not a result of position within a CH or distance from its edge.

In the case of Coulomb friction with H dragging heavy ions out of the corona, Bodmer & Bochsler (1998, 2000) show that there is a mass dependence and the associated fractionation would be stronger in slow than fast wind. Such a trend does not agree with the fractionation we observe in fast wind and lack of fractionation in slow wind when FIP fractionation is accounted for by normalizing abundances to A_s . As such, we rule out Coulomb friction as a source of the observed $v > v_s$ trend.

Rivera et al. (2021) report signatures of mass-dependent fractionation in CMEs in which heavy ion abundances decrease with increasing mass when absolute CME abundances (X/H) are normalized to ambient absolute solar wind abundances. Lepri & Rivera (2021) report a similar trend for prominence material, though of higher values. Rivera et al. (2021) attribute this trend to gravitational settling. Weberg et al. (2012) also demonstrate that gravitational settling leads to mass-dependent fractionation in ambient solar wind. However, gravitational settling has a timescale on the order of days and requires closed loops, which are common in equatorial regions where slow wind originates, not CH regions from which fast wind is from. As such, the mass-dependent fractionation observed in solar wind with speeds $v > v_s$ is also unlikely due to gravitational settling.

In short, we have shown that the observed fast wind enhancements of heavy ion abundances above A_s and the corresponding mass-dependent fractionation are inconsistent with the effects of gravitational settling, H dragging coronal heavy ions into the solar wind by means of Coulomb friction, and gradients across CHs. Pilleri et al. (2015) suggest that mass-dependent fractionation is consistent with a pondermotive-driven FIP effect. Although our trends qualitatively agree with Pilleri et al. (2015), Laming (2004, 2009, 2015) explicitly state that a pondermotive-

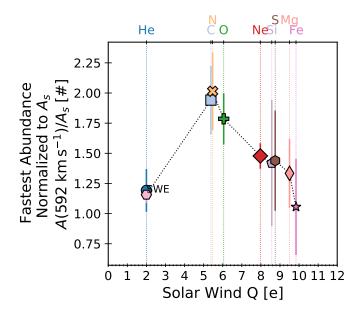


Fig. 8. The abundance at $v_{\rm sw}=592~{\rm km\,s^{-1}}$ normalized to A_s as a function of solar wind charge state. Excluding He, the decreasing trend with increasing M indicates a heavy ion fractionation process in fast solar wind.

driven FIP effect is mass independent. As such, this may be novel mass-dependent, fast wind fractionation or the fractionation depends on a different quantity.

In addition to FIP and M, the elements reported here are summed over a series of charge states and, as such, have an average charge state. Renaud & Victoria-Feser (2010, Eq. (14)) propose a robust coefficient of determination (R_w^2) that is appropriate for rapidly determining if a model reasonably fits a set of data that includes uncertainties. Excluding He, we have fit the fastest abundances observed $A\left(592~\mathrm{km\,s^{-1}}\right)/A_s$ as a function of FIP, M, solar wind charge state Q (von Steiger et al. 1997; Desai et al. 2006), M/Q, and M^2/Q^2 with a line and calculated R_w^2 as a simple means of quantifying how well-organized $A\left(592~\mathrm{km\,s^{-1}}\right)/A_s$ is by each quantity. All R_w^2 are < 0.55 except for the dependence on average charge state, for which $R_w^2=0.95$. Figure 8 plots $A\left(592~\mathrm{km\,s^{-1}}\right)/A_s$ as a function of charge state in the style of Figures 4 and 6. Although we do not have an explanation for this result, it suggests that the fractionation may depend on solar wind charge state.

Beyond the reported M- or Q-dependent fractionation of $A(v > v_s)/A_s$, Figure 3 shows that the degree of fractionation increases with v_{sw} for $v > v_s$. To achieve the asymptotically fastest speeds observed at 1 AU, energy must be deposited into the solar wind above the sonic critical point r_c (Leer & Holzer 1980; Hansteen & Velli 2012). The faster the speed before this yetto-be-identified mechanism accelerates the solar wind and the more energy deposited by it, the larger the asymptotic speed. Recent work (Rivera et al. 2024b; Bale et al. 2023; Raouafi et al. 2023) shows that the solar wind's acceleration at distances $r > r_A$ is driven by the deposition of energy into the solar wind from switchbacks dissipation during solar wind propagation through interplanetary space. Given all ions are observed at fast wind speeds that the solar wind requires such energy deposition to reach, the increase in the degree of heavy ion fractionation may indicate that there is a preferential coupling between these heavy ions and the energy deposition process. On the other hand, we have argued that the consistency of v_s across the heavy ions suggests that $v_{s,\text{He}} > v_{s,\text{Heavy}}$ may indicate He is impacted by this yet-to-be-identified acceleration mechanism at distances from the sun above r_c and heavier elements are not. If this is the case, then the dependence of the fractionation process for $v > v_s$ must be located at or near r_c .

5. Conclusion

Under the two-state paradigm, the solar wind is classified into fast and slow based on whether its speed is above or below a threshold value. This threshold is typically between ~ 400 and $\sim 600 \text{ km s}^{-1}$ and chosen in an *ad hoc* or heuristic fashion. Fast solar wind with speeds above this threshold value are typically observed to come from magnetically open, typically polar regions like coronal holes (CHs) (Phillips et al. 1994; Geiss et al. 1995b). Slow solar wind is from more equatorial regions with magnetic fields that may only be intermittently open to the heliosphere (Fisk et al. 1999; Subramanian et al. 2010; Antiochos et al. 2011; Crooker et al. 2012; Abbo et al. 2016; Antonucci et al. 2005). Analysis of the solar wind's kinetic (Kasper et al. 2008, 2017; Tracy et al. 2016; Kasper et al. 2006; Fu et al. 2018; Stakhiv et al. 2016; Alterman et al. 2018), heavy ion abundance along with charge-state ratio (von Steiger et al. 2000; Geiss et al. 1995b,a; Zhao et al. 2017a, 2022; Xu & Borovsky 2015; Fu et al. 2017, 2015), Alfvénicity (D'Amicis et al. 2021b,a; Bruno & Carbone 2013; Tu & Marsch 1995), and heavy ion composition in switchbacks (Rivera et al. 2024a) provide a more nuanced picture in which there are multiple classes of solar wind.

Motivated by the distinct gradients of He/H as a function of $v_{\rm sw}$ observed by Wind/SWE above and below the speed $v_{\rm s}$, we have investigated the variation of X/H observed by ACE/SWICS as a function of $v_{\rm sw}$. We have made the following observations and inferences.

- 1. All species have two distinct gradients as a function of v_{sw} and these gradients are shallower above the speed v_s . From this, we infer that the change in gradients is a signature of differences in the magnetic topology at distinct types of solar wind source regions.
- 2. The He saturation speed is $v_s = 399 \pm 2 \text{ km s}^{-1}$ (observed by SWE) and $v_s = 390 \pm 4 \text{ km s}^{-1}$ (observed by SWICS). We interpret this as showing that SWE and SWICS He/H are statistically consistent over the years 1998 to 2011.
- 3. The average v_s across elements heavier than He is $v_s = 327 \pm 2 \text{ km s}^{-1}$, independent of species, which is $63 \pm 4.5 \text{ km s}^{-1}$ slower than v_s for SWICS' He/H. Moreover, the speed v_s for heavy elements is slower than the peak of the solar wind distribution and the speed v_s for He is faster than the peak of the solar wind distribution. From this, we infer that He may be impacted by the acceleration at heights above the sonic point that is necessary for non-transient solar wind to reach the asymptotically fastest speeds observed at 1 AU and heavy elements are not.
- 4. If our inferences about the change in gradients of X/H as a function of v_{sw} across v_s and the observation that $v_{s,He} > v_{s,Heavy}$ hold, then this implies that setting a threshold for differentiating between slow and fast solar wind in the range of 400 to 600 km s⁻¹ may lead to a "slow" solar wind with a chemical makeup that is a mixture of solar wind from CH and equatorial regions that are only intermittently open to the heliosphere.
- 5. The saturation abundances A_s at the speed v_s are ordered by FIP and show an expected fractionation pattern. From this,

- we unsurprisingly infer that the fast/slow solar wind transition is the result of a mechanism that impacts the solar wind at heights above chromosphere, above where processes like the pondermotive force that would fractionates the solar plasma occur.
- 6. When normalized to the point (v_s, A_s) , the gradients for elements heavier than He are indistinguishable for $v < v_s$. We interpret this observation as a signature that there is not a mechanism preferentially coupled to and driving slow wind abundance gradients as a function of species.
- 7. When normalized to the point (v_s, A_s) , the gradients for elements heavier than He are indistinguishable for $v > v_s$ are ordered by M or average solar wind Q for $v > v_s$. Although average charge state provides a better ordering of the ratio of the fastest reported abundances to the saturation abundances $A(592 \text{ km s}^{-1})/A_s$ as indicated by the weighted coefficient of determination, such a fractionation process that only depends on average charge state is difficult to justify. Even though we have ruled out multiple mass-dependent mechanisms as possible sources of the observed fractionation at speeds $v > v_s$, this leaves such a charge state dependent fractionation unsatisfying.

The bimodal nature of the solar wind's distribution is most pronounced during solar minima when coronal holes are restricted to the Sun's polar regions and its equatorial regions are dominated by helmet streamers, pseudostreamers, and other features with magnetic topologies that are not connected to the heliosphere in a simple, radial fashion. Furthermore, additional properties like the solar wind's Alfvénicity have shown that there is solar wind with speeds that are traditionally considered to be slow, but fast wind kinetic, chemical, and charge state properties. This Alfvénic slow wind believed to emanate from coronal holes and not equatorial sources. Further analysis of the solar wind's chemical makeup and its variation as a function of Alfvénicity and solar activity should provide additional insight into the relationship between *in situ* solar wind observations and their sources on the Sun.

Acknowledgements. The authors thank Ruth Skokie for discussions of ACE/SWEPAM data. BLA acknowledges NASA Grants 80NSSC22K0645 (LWS/TM), 80NSSC22K1011 (LWS), and 80NSSC20K1844. YJR acknowledges support from the Future Faculty Leaders postdoctoral fellowship at Harvard University. JMR and STL acknowledge NASA contract 80NSSC23K0542 (ACE/SWICS).

References

- Abbo, L., Ofman, L., Antiochos, S. K., et al. 2016, Space Science Reviews, 201, 55, tex.ids= Abbo2016a
- Acuña, M. H., Ogilvie, K. W., Baker, D. N., et al. 1995, Space Science Reviews, 71, 5
- Aellig, M. R., Lazarus, A. J., & Steinberg, J. T. 2001, Geophysical Research Letters, 28, 2767
- Alterman, B. L., Desai, M. I., Dayeh, M. A., Mason, G. M., & Ho, G. 2023, The Astrophysical Journal, 952, 42
- Alterman, B. L. & Kasper, J. C. 2019, The Astrophysical Journal, 879, L6, publisher: IOP Publishing
- Alterman, B. L., Kasper, J. C., Leamon, R. J., & McIntosh, S. W. 2021, Solar Physics, 296, 67, arXiv: 2006.04669 Publisher: The Author(s), under exclusive licence to Springer Nature B.V. ISBN: 1120702101801
- Alterman, B. L., Kasper, J. C., Stevens, M., & Koval, A. 2018, The Astrophysical Journal, 864, 112, publisher: IOP Publishing
- Antiochos, S. K., Mikic, Z., Titov, V. S., Lionello, R., & Linker, J. A. 2011, The Astrophysical Journal, 112, arXiv: 1102.3704 tex.ids= Antiochos2011a
- Antonucci, E., Abbo, L., & Dodero, M. A. 2005, Astronomy & Astrophysics, 435, 699
- Asplund, M., Amarsi, A. M., & Grevesse, N. 2021, Astronomy & Astrophysics, 653, A141

- Baker, D., Démoulin, P., Yardley, S. L., et al. 2023, The Astrophysical Journal, 950, 65
- Bale, S. D., Drake, J. F., McManus, M. D., et al. 2023, Nature, 618, 252
- Bodmer, R. & Bochsler, P. 1998, Physics and Chemistry of the Earth, 23, 683Bodmer, R. & Bochsler, P. 2000, Journal of Geophysical Research: Space Physics, 105, 47
- Borovsky, J. 2016, Journal of Geophysical Research A: Space Physics, 121, 5055, iSBN: 2169-9402 tex.ids= Borovsky2016a, Borovsky2016b
- Brooks, D. H., Ugarte-Urra, I., & Warren, H. P. 2015, Nature Communications, 6, publisher: Nature Publishing Group
- Bruno, R. & Carbone, V. 2013, Living Reviews in Solar Physics, 10, 1
- Burnett, D. S., Barraclough, B. L., Bennett, R., et al. 2003, Space Science Reviews, 105, 509, iSBN: 0038-6308
- Crooker, N. U., Antiochos, S. K., Zhao, X., & Neugebauer, M. 2012, Journal of Geophysical Research: Space Physics, 117, n/a, iSBN: 0148-0227
- D'Amicis, R. & Bruno, R. 2015, Astrophysical Journal, 805, 1, publisher: IOP Publishing ISBN: 1538-4357
- Del Zanna, G. 2019, Astronomy & Astrophysics, 624, A36
- Desai, M., Mason, G., Gold, R. E., et al. 2006, The Astrophysical Journal, 649, 470
- Doschek, G. A. & Warren, H. P. 2019, The Astrophysical Journal, 884, 158
- Du, Z. 2012, Solar Physics, 278, 203, arXiv: 1112.5560 ISBN: 1573-093X
- D'Amicis, R., Alielden, K., Perrone, D., et al. 2021a, Astronomy & Astrophysics, 654, A111
- D'Amicis, R., Perrone, D., Bruno, R., & Velli, M. 2021b, Journal of Geophysical Research: Space Physics, 126
- Feldman, U. & Laming, J. M. 2000, Physica Scripta, 61, 222
- Feldman, W. C., Asbridge, J. R., Bame, S. J., & Gosling, J. T. 1978, Journal of Geophysical Research, 83, 2177
- Fisk, L. A., Zurbuchen, T. H., & Schwadron, N. A. 1999, The Astrophysical Journal, 521, 868
- Fu, H., Li, B., Li, X., et al. 2015, Solar Physics, 290, 1399
- Fu, H., Madjarska, M. S., Li, B., Xia, L., & Huang, Z. 2018, Monthly Notices of the Royal Astronomical Society, 478, 1884
- Fu, H., Madjarska, M. S., Xia, L., et al. 2017, The Astrophysical Journal, 836, 169
- Geiss, J. 1982, Space Science Reviews, 33, 201, iSBN: 9783540773405
- Geiss, J., Gloeckler, G., & von Steiger, R. 1995a, Space Science Reviews, 72, 49
 Geiss, J., Gloeckler, G., Von Steiger, R., et al. 1995b, Science, 268, 1033, publisher: Physikalisches Institut, University of Bern, Switzerland. tex.ids=
- Gloeckler, G., Cain, J., Ipavich, F. M., et al. 1998, Space Sci. Rev., 86, 497, publisher: Kluwer Academic Publishers
- Hansteen, V. H. & Velli, M. 2012, Space Science Reviews, 172, 89
- Hathaway, D. H. 2015, Living Reviews in Solar Physics, 12, iSBN: 1614-4961Hewins, I. M., Gibson, S. E., Webb, D. F., et al. 2020, Solar Physics, 295, publisher: Springer Nature B.V.
- Hirshberg, J. 1973, Reviews of Geophysics, 11, 115
- Holzer, T. E. & Leer, E. 1980, Journal of Geophysical Research: Space Physics, 85, 4665
- Holzer, T. E. & Leer, E. 1981, in Solar Wind 4 (Burhausen, Germany: Max Planck Institut f\u00fcr Aeronomie and Max Planck Institut f\u00fcr exraterrestriesche Physik), 28-41, conference Name: Solar Wind 4 Pages: 28 ADS Bibcode: 1981sowi.conf...28H
- Johnson, M., Rivera, Y. J., Niembro, T., et al. 2024, The Astrophysical Journal, 964, 81
- Johnstone, C. P., Güdel, M., Lüftinger, T., Toth, G., & Brott, I. 2015, Astronomy & Astrophysics, 577, A27
- Kasper, J. C. 2002, PhD thesis, Massachusetts Institute of Technology
- Kasper, J. C., Klein, K. G., Lichko, E., et al. 2021, Physical Review Letters, 127, 255101
- Kasper, J. C., Klein, K. G., Weber, T., et al. 2017, The Astrophysical Journal, 849, 126
- Kasper, J. C., Lazarus, A. J., & Gary, S. P. 2008, Physical Review Letters, 101, 261103
- Kasper, J. C., Lazarus, A. J., Steinberg, J. T., Ogilvie, K. W., & Szabo, A. 2006, Journal of Geophysical Research, 111, A03105
- Kasper, J. C., Stevens, M., Lazarus, A. J., Steinberg, J. T., & Ogilvie, K. W. 2007, The Astrophysical Journal, 660, 901
- Kasper, J. C., Stevens, M. L., Korreck, K. E., et al. 2012, The Astrophysical Journal, 745, 162
- Klein, K. G., Alterman, B. L., Stevens, M., Vech, D., & Kasper, J. C. 2018, Physical Review Letters, 120, 205102, publisher: American Physical Society Laming, J. M. 2004, The Astrophysical Journal, 614, 1063
- Laming, J. M. 2009, The Astrophysical Journal, 695, 954
- Laming, J. M. 2012, The Astrophysical Journal, 744, 115, arXiv: astro-ph.SR/1110.4357
- Laming, J. M. 2015, Living Reviews in Solar Physics, 12, arXiv: 1504.08325 ISBN: 2367-3648

- Leer, E. & Holzer, T. E. 1980, Journal of Geophysical Research: Space Physics, $85,4681\,$
- Lepri, S. T., Landi, E., & Zurbuchen, T. H. 2013, The Astrophysical Journal, 768,
- Lepri, S. T. & Rivera, Y. J. 2021, The Astrophysical Journal, 912, 51, publisher: IOP Publishing tex.ids= Lepri2021a, Lepri2021b
- Livi, S. A., Möbius, E., Haggerty, D., Witte, M., & Wurz, P. 2003, AIP Conference Proceedings, 679, 850, iSBN: 0735401489
- Marsch, E. 2006, Advances in Space Research, 38, 921
- Martinović, M., Klein, K. G., Durovcova, T., & Alterman, B. L. 2021, 1, arXiv: 2110.07772
- Martinović, M., Klein, K. G., Kasper, J. C., et al. 2020, The Astrophysical Journal Supplement Series, 246, 30, arXiv: 1912.02653
- Maruca, B. A. & Kasper, J. C. 2013, Advances in Space Research, 52, 723, publisher: COSPAR
- Mason, G. M., Desai, M., & Li, G. 2012, Astrophysical Journal Letters, 748, 2010
- McComas, D. J., Ebert, R. W., Elliott, H. A., et al. 2008, Geophysical Research Letters, 35, L18103
- McIntosh, S. W., Kiefer, K. K., Leamon, R. J., Kasper, J. C., & Stevens, M. 2011, Astrophysical Journal Letters, 740, 1, arXiv: 1109.1408
- McIntosh, S. W., Leamon, R. J., Krista, L. D., et al. 2015, Nature Communications, 6, 1, publisher: Nature Publishing Group ISBN: 2041-1723 (Electronic)\r2041-1723 (Linking)
- Meyer-Vernet, N. 2007, Basics of the Solar Wind, 1st edn. (Cambridge University Press)
- Mihailescu, T., Brooks, D. H., Laming, J. M., et al. 2023, The Astrophysical Journal, 959, 72
- Nicolaou, G., Livadiotis, G., & Moussas, X. 2014, Solar Physics, 289, 1371
- Ogilvie, K. W., Chornay, D. J., Fritzenreiter, R. J., et al. 1995, Space Science Reviews, 71, 55
- Parker, E. N. 1958, The Astrophysical Journal, 128, 664, iSBN: 9780874216561Phillips, J. L., Balogh, A., Bame, S. J., et al. 1994, Geophysical Research Letters, 21, 1105
- Pilleri, P., Reisenfeld, D. B., Zurbuchen, T. H., et al. 2015, The Astrophysical Journal, 812, 1
- Pottasch, S. R. 1963, The Astrophysical Journal, 137, 945
- Raouafi, N. E., Stenborg, G., Seaton, D. B., et al. 2023, The Astrophysical Journal, 945, 28
- Raymond, J. C., Kohl, J. L., Noci, G., et al. 1997, in The First Results from SOHO, ed. B. Fleck & Z. Švestka (Dordrecht: Springer Netherlands), 645– 665
- Reisenfeld, D. B., Wiens, R. C., Barraclough, B. L., et al. 2013, Space Science Reviews, 175, 125
- Renaud, O. & Victoria-Feser, M.-P. 2010, Journal of Statistical Planning and Inference, 140, 1852
- Richardson, I. G. & Cane, H. V. 2010, Solar Physics, 264, 189
- Rivera, Y. J., Badman, S. T., Stevens, M. L., et al. 2024a, The Astrophysical Journal, 974, 198
- Rivera, Y. J., Badman, S. T., Stevens, M. L., et al. 2024b, Science, 385, 962
- Rivera, Y. J., Higginson, A., Lepri, S. T., et al. 2022a, Frontiers in Astronomy and Space Sciences, 9, 1056347
- Rivera, Y. J., Landi, E., Lepri, S. T., & Gilbert, J. A. 2020, The Astrophysical Journal, 899, 11
- Rivera, Y. J., Lepri, S. T., Raymond, J. C., et al. 2021, The Astrophysical Journal, 921, 93
- Rivera, Y. J., Raymond, J. C., Landi, E., et al. 2022b, The Astrophysical Journal, 936, 83
- Schwadron, N. A., Fisk, L. A., & Zurbuchen, T. H. 1999, The Astrophysical Journal, 521, 859
- Schwenn, R. 2006, Space Science Reviews, 124, 51
- Shearer, P., von Steiger, R., Raines, J. M., et al. 2014, The Astrophysical Journal, 789, 60
- Song, H. Q., Zhang, J., Cheng, X., et al. 2020, The Astrophysical Journal, 901, L21, arXiv: 2009.05212
- Stakhiv, M. O., Landi, E., Lepri, S. T., Oran, R., & Zurbuchen, T. H. 2015, The Astrophysical Journal, 801, 100
- Stakhiv, M. O., Lepri, S. T., Landi, E., Tracy, P. J., & Zurbuchen, T. H. 2016, The Astrophysical Journal, 829, 117, publisher: IOP Publishing ISBN: 0769518745
- Stone, E. C., Frandsen, A. M., Mewaldt, R. A., et al. 1998, Space Science Reviews, 86, 1, publisher: Kluwer Academic Publishers ISBN: 10.1023/A:1005082526237
- Subramanian, S., Madjarska, M. S., & Doyle, J. G. 2010, Astronomy and Astrophysics, 516, A50
- Tlatov, A., Tavastsherna, K., & Vasil'eva, V. 2014, Solar Physics, 289, 1349
- Tracy, P. J., Kasper, J. C., Raines, J. M., et al. 2016, Physical Review Letters, 255101, 255101
- Tu, C. Y. & Marsch, E. 1995, Space Science Reviews, 73, 1, iSBN: 0038-6308

- Verscharen, D., Klein, K. G., & Maruca, B. A. 2019, The multi-scale nature of the solar wind, Vol. 16 (Springer International Publishing), arXiv: 1902.03448 Publication Title: Living Reviews in Solar Physics Issue: 1 ISSN: 16144961
- Viall, N. M. & Borovsky, J. 2020, Journal of Geophysical Research: Space Physics, 125, 1
- von Steiger, R., Geiss, J., & Gloeckler, G. 1997, in Cosmic Winds and the Heliosphere, Space Science Series, 581–611, conference Name: Cosmic Winds and the Heliosphere Pages: 581 ADS Bibcode: 1997cwh..conf..581V
- von Steiger, R., Schwadron, N. A., Fisk, L. A., et al. 2000, Journal of Geophysical Research: Space Physics, 105, 27217
- Von Steiger, R. & Zurbuchen, T. H. 2016, The Astrophysical Journal, 816, 13 Wang, Y. M. & Sheeley, N. R. 2002, Journal of Geophysical Research: Space Physics, 107, 1
- Weberg, M. 2015, Spatial and Temporal Coordinate Systems in Space Physics, Tech. rep.
- Weberg, M., Zurbuchen, T. H., & Lepri, S. T. 2012, Astrophysical Journal, 760 Widing, K. G. & Feldman, U. 2001, The Astrophysical Journal, 555, 426
- Wurz, P., Bochsler, P., & Lee, M. A. 2000, Journal of Geophysical Research: Space Physics, 105, 27239
- Xu, F. & Borovsky, J. 2015, Journal of Geophysical Research: Space Physics, 120, 70
- Yogesh, Chakrabarty, D., & Srivastava, N. 2021, Monthly Notices of the Royal Astronomical Society: Letters, 503, L17, publisher: Oxford University Press Yogesh, Chakrabarty, D., & Srivastava, N. 2023, Monthly Notices of the Royal
- Astronomical Society, 526, L13

 Zerbo, J.-L. & Richardson, J. D. 2015, Journal of Geophysical Research: Space Physics, 120, 10,250
- Zhao, L., Landi, E., Lepri, S. T., & Carpenter, D. 2022, Universe, 8, 393
- Zhao, L., Landi, E., Lepri, S. T., et al. 2017a, The Astrophysical Journal, 846, 135, publisher: IOP Publishing
- Zhao, L., Zhang, M., & Rassoul, H. K. 2017b, The Astrophysical Journal, 836, 31, publisher: IOP Publishing
- Zurbuchen, T. H. & Richardson, I. G. 2006, Space Science Reviews, 123, 31
- Zurbuchen, T. H., Weberg, M., Von Steiger, R., et al. 2016, The Astrophysical Journal, 826, 10